Journal of the Brazilian Society of Mechanical Sciences and Engineering (2019) 41:368
https://doi.org/10.1007/s40430-019-1859-8

TECHNICAL PAPER

Successive melting and solidification of paraffin–alumina nanomaterial in a cavity as a latent heat thermal energy storage

R. Yadollahi Farsani[1] · A. Raisi[2] · Amirhoushang Mahmoudi[3]

Received: 13 November 2018 / Accepted: 2 August 2019 / Published online: 20 August 2019

Abstract

Latent heat thermal energy storage (LHTES) plays a main role in many industrial applications, especially in high-powered electronics cooling systems and providing the thermal energy demand when the energy supply is unavailable. In this study, the LHTES cycle process, including successive melting and solidification, investigates in a two-dimensional annular space of a square cavity filled with nanomaterial of paraffin–alumina as a nanoPCM. In the melting process, all sidewalls of the cavity are insulated. Meanwhile, a constant heat rate generates homogeneously within the central heat source. At the end of melting, the heat generation gets off, while a time-reducing temperature lower than the paraffin melting point imposes on the sidewalls, and then, solidification triggers. The numerical simulation was accomplished using control volume method and the governing equations solved using the SIMPLE algorithm. The enthalpy-porosity method was employed to model the phase-change front. The value of thermal conductivity and the viscosity of the nanofluid have been experimentally measured before the numerical modeling. In this study, the effect of volume fraction of nanoparticles (0–0.03) has been investigated on the successive melting and solidification rate for a constant Rayleigh number of 5.74×10^5. The results show that adding nanoparticles to the PCM equal to the volume fractions of 0.01 and 0.02 improves melting rate, but the nanofluid with the volume fraction of 0.03 represents a poor heat transfer rate during melting even weaker than those for nanofluid with the volume fraction of 0.01. It also observed that the nanomaterial with the volume fraction of $\varphi = 0.03$ represents the highest solidification rate. However, taking the overall performance of successive melting and solidification system into account, the nanofluid with the volume fraction of 0.02 remarked the most effective heat transfer rate in comparison with the other examined cases.

Keywords Successive melting and solidification · PCM · LHTES · Nanomaterial · Paraffin · Alumina

List of symbols

b	Enthalpy-porosity coefficient (kg m^{-3} s^{-1})
B	Dimensionless enthalpy-porosity coefficient
B_z	Boltzmann constant
c	Specific heat (J kg^{-1} K^{-1})
f	Liquid fraction
g	Gravity (m s^{-2})
h	Enthalpy (J kg^{-1} K^{-1})
L, l	Cavity and heat source dimension (m)
k	Thermal conductivity (W m^{-1} K^{-1})
Nu	Nusselt number, $-k_{nf}/k_f(T_s - T_m)\partial T/\partial n$
p	Pressure (N m^{-2})
P	Dimensionless pressure
Pr	Prandtl number, $Pr = \nu_f/\alpha_f$
q'''	Heat generation rate (W m^{-3})
Ra	Rayleigh number, $g\beta_f q''' l^5/\nu_f \alpha_f k_s$
Ste	Stefan number, $c_f q''' l^2/h_{nf} k_s$
T	Temperature (K)
T_m, T_s	Melting and solidification points (K)
T_h, T_c	Hot and cold temperatures (K)
t	Time (s)
u, v	Velocity in the x, y direction (m s^{-1})
U, V	Dimensionless velocity
x, y	Cartesian coordinate (m)
X, Y	Dimensionless Cartesian coordinate

Technical Editor: Francis HR Franca, Ph.D.

✉ R. Yadollahi Farsani
r.yadollahi@iaushk.ac.ir; raul.yfa@gmail.com

[1] Department of Mechanical Engineering, Shahrekord Branch, Islamic Azad University, Shahrekord, Iran

[2] Faculty of Engineering, Shahrekord University, Shahrekord, Iran

[3] Department of Thermal and Fluid Engineering, University of Twente, Enschede, The Netherlands

Abbreviations

CLF	Cavity liquid fraction
PCM	Phase-change material
NePCM	Nano-enhanced PCM

Greek symbols

α	Thermal diffusivity ($m^2\ s^{-1}$)
β	Expansion coefficient (K^{-1})
μ	Dynamic viscosity ($N\ s\ m^{-2}$)
ν	Kinematic viscosity ($m^2\ s^{-1}$)
θ	Dimensionless temperature
ρ	Density ($kg\ m^{-3}$)
ϕ	Volume fraction
σ	Electrical conduction ($S\ m^{-1}$)
τ	Dimensionless time

Subscripts

f, s	Fluid and solid
m	Melting point
nf	Fluid PCM with nanoparticles
ns	Solid PCM with nanoparticles
np	Nanoparticles

1 Introduction

Recently, the solar energy and the corresponding technical components such as receivers, solar collectors, and thermal energy storages (TESs) have sparked a heated debate [1]. TESs are integral parts of solar power plants that store thermal energy and release it in another time for heating, cooling, and power generation. Since heat demand fluctuates during the day and also from day to day, a storage device would be beneficial to provide balance between supply and demand of energy [2]. TESs, on the one hand, play an important role in reducing the peak consumption and emissions of greenhouse gases. On the other hand, they increase the efficiency of energy systems [3]. Therefore, such issue deserves to be taken more into consideration.

From the amount of heat-stored standpoint, phase-change material (PCM) can store or release a large amount of latent heat during the melting and solidification processes due to a large enthalpy amount of phase changing that is usually more than 100–200 times the sensible heat. Moreover, unlike a sensible storage device that experiences high temperature changes during the thermal absorption and release processes, a TES system integrated with a PCM, namely latent heat thermal energy storage (LHTES), operates in an almost isotherm process [4]. Table 1 shows the thermal properties of some commercial PCMs [5].

Despite the high thermal efficiency of PCMs, their main downside is having low thermal conductivity, which is typically about 0.2–0.7 $W\ m^{-1}\ K^{-1}$ [6]. This is especially more significant during the solidification process, where solidification occurs initially at boundaries, and then, the solidified phase itself acts as an insulation between the heat source and solidification front. In the melting process, buoyancy-driven flows and natural convections play the main role in the heat transfer from a heat source to the melting front [7].

The time of absorbing and releasing heat, which is directly associated with heat transfer rate, is one of the essential factors in the design of a TES [8]. Over the past years, researchers have done many studies on the ways of increasing the heat transfer rate. Therefore, several methods have been proposed. One is the addition of solid nanoparticles with a high thermal conductivity coefficient to the PCM [9]. In particular, a close-contact melting and solidification of PCM equipped with nanoparticles have been exponentially assigned by researchers [10–14].

One study carried out by Feng et al. [15] on melting in a cavity with a heated bottom was numerically modeled using the lattice Boltzmann method (LBM). In this study, the phenomenon of ice including copper nanoparticles melting was conducted. Their results were presented in the form of streamlines and isotherms of the various nanoPCM compositions ($\varphi = 0, 0.01, 0.05$) and different Grashof numbers $\left(Gr = 2.5 \times 10^5, 5 \times 10^5\right)$. The results show that the addition of copper nanoparticles to the PCM increases the heat transfer efficiency in the melting process. In other words, an increase in the solid volume fraction increases the melting rate as well as the stored energy capacity.

Arici et al. [16] investigated the phenomenon of the melting of paraffin–alumina nanoPCM in a rectangular cavity with partially heated and cooled walls. The results show that the highest melting rate occurs for a nanoPCM with $\varphi = 0.01$. Furthermore, the best thermal performance is obtained when the enclosure is heated from the bottom.

Table 1 Thermal properties of some commercial PCMs [5]

PCM	Melting point (°C)	Density ($kg\ m^{-3}$)	Thermal conductivity ($W\ m^{-1}\ K^{-1}$)	Special heat ($kJ\ kg^{-1}\ K^{-1}$)	Latent heat ($kJ\ kg^{-1}$)
Paraffin RT44	41–45	780	0.20	2.0	255
E117 non-organic	117	1450	0.70	2.61	245
Organic A164	164	1500	Unknown	Unknown	459
$NANO_3$	307	2260	0.5	Unknown	389
KNO_3	333	2110	0.5	Unknown	477

After 30 min from the start of the melting process, the liquid volume fraction and the stored energy for the case with the bottom-heated cavity are increased at least 16% and 9%, respectively, compared to the side-heated cavity.

Sebti et al. [17] numerically studied the melting of paraffin–copper nanoPCM in a square cavity. They used the enthalpy-porosity technique to follow the melting front. Based on the results, the addition of copper nanoparticles to the base material affected the melting rate through the increase in thermal conductivity of the material. This effect led to an increase in the melting rate with an increase in the nanoparticles volume fraction.

Farsani et al. [18] investigated the influence of adding alumina nanoparticles to paraffin wax on the melting phenomena in a cavity including a heat source at its center. The results show that, for the considered configuration, the addition of nanoparticles for 0.01 and 0.02 volume fraction of alumina nanoparticles does not remark any significant influence on the melting rate of the PCM, which is contrary to the observations with other geometries in the literature. For the nanoPCMs with the 0.04 and 0.05 volume fractions, a relative decrease in the melting rate of the nanoPCM was reported.

Darzi et al. [19] examined the melting process of water–copper nanoPCM due to the natural convection heat transfer in an insulated cavity in which an isotherm heat source was located. They used the LBM to perform the simulation. The effect of the location of the isotherm heat source inside the cavity was also investigated. The results show that an increase in the nanoparticles volume fraction from 0 to 4% increases the melting rate by 52.7, 41.2, and 30%, when the heat source is located at the top, center, and bottom of the cavity, respectively.

Boukani et al. [20] investigated the melting of the nanoPCM of n-octadecane paraffin dispersed with Cu nanoparticles in partially filled horizontal elliptical capsules with different aspect ratios. The different aspect ratios and nanoparticles volumetric concentrations have been considered. The simulations were carried out using the enthalpy-porosity technique and volume of fraction (VOF) model. The results show that an increase in nanoparticles volume fraction enhances the melting rate but decreases the nanoPCM volume change. In addition, the highest and the lowest melting rates are associated with the aspect ratio of 2.0 and 1.0, respectively.

Kashani et al. [21] studied numerically the thermal behavior of solidification of water–copper nanofluid in a two-dimensional cavity with wavy vertical walls. The effect of the wavy wall and natural convection, as well as the nanoparticles volume fraction on the solidification time, was investigated. The results were obtained for a wide range of Grashof numbers and nanoparticles volume fractions. They neglected supercooling as well as the effect of nanoparticles dispersion on the solidification point. However, it is well known that in the process of water freezing the supercooling phenomenon exists. They employed the enthalpy-porosity method for the numerical study of the solidification. This method has been used for many years for modeling melting and solidification. Their results show that the natural convection increases with the increase in the nanoparticles volume fraction and the Grashof number. This leads to an increase in the Nusselt number.

Sheikholeslami [11] studied the solidification process within the space between an aluminum inner sinusoidal fin and elliptic storage tank, filled with CuO–water nanofluid, using finite element method. The effect of the amplitude value of the fin, the volume fraction of nanofluid, and the diameter of nanoparticles on the solidification rate was simulated. The results proved that solidification rate is improved by adding CuO nanoparticles to the pure PCM.

Khodadadi and Fan [22] analyzed the effect of adding different nanoparticles to water and cyclohexane using Stefan method. They calculated the solidification time for different concentrations and concluded that the solidification time decreases by increasing the concentration of nanoparticles in each of the examined materials. However, the results of this study showed that for a basic fluid and a constant volume fraction, the non-dimensional solidification time for different nanoparticles is almost the same.

To model numerically the heat transfer within nanofluids, some basic thermal properties such as thermal conductivity and viscosity are calculated using classical equations. Maxwell equation [23, 24] and Einstein relation [25] are the well-known samples. Each of them is validated under specific and limited conditions. Moreover, the effect of some important parameters like the nanoparticles size and their distribution has not usually been considered. On the other hand, LHTES has been innovated to experience a long-term process of heat charging and discharging sequentially. In a real application, based on this, melting and solidification processes happen one after another. Therefore, in this study, firstly, the thermal conductivity and dynamic viscosity of paraffin–Al_2O_3 nanofluids are calculated empirically and then substituted in the governing equations. Secondly, a successive melting and solidification process of paraffin–alumina nanoPCM within the annular space located between a square heat source and cavity walls are investigated numerically. To the best knowledge of us, the previous studies have not considered this new feature of LHTES system.

2 Statement of the problem

As it is shown in Fig. 1a, the annular space between the aluminum heat source and the cavity walls is assumed to be filled with paraffin–alumina nanoPCM in the solid phase with the

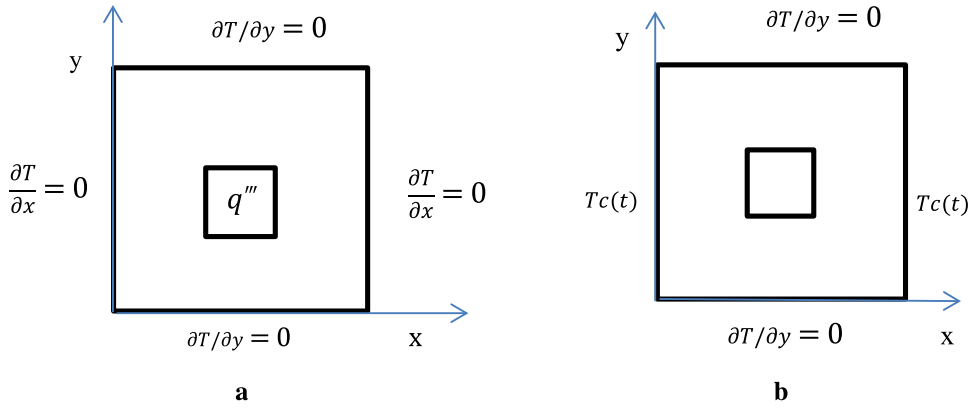

Fig. 1 Schematic view of the computational domain. **a** (Melting case): with a heat source at the center and insulated sidewalls. **b** (Solidification case): the cavity including the solid block at the center with cold sidewalls

Table 2 Thermophysical properties of the paraffin [26], Al_2O_3 [27], and aluminum at $T = 300$ K

Property	Paraffin	Al_2O_3	Al
Viscosity, μ_f (Ns m^{-2})	$\mu_o(T) = 0.07193e^{-0.0365T}$	–	–
Density, ρ_f (ρ_s) (kg m^{-3})	860	3600	2700
Thermal expansion coefficient, β (K^{-1})	1.0 (10^{-3})	1.6 (10^{-5})	–
Thermal conductivity, k_f (k_s) (W m^{-1} K^{-1})	0.14	36	202
Melting point, T_m (°C)	− 12	–	60.32
Latent heat fusion, h_m (J kg^{-1})	200,000	–	–
Specific heat, c_f (c_s) (J kg^{-1} K^{-1})	2000 (2000)	765	903

homogeneous temperature equal to its melting point. Dimensions of the cavity and heat source are given in Fig. 1. In the case of melting, all the sidewalls of the cavity are insulated, while the heat source generates heat with a constant heat rate of q''' per volume unit of the heat source. The melting of the nanoPCM begins along the heat source and gradually covers the entire cavity. During the melting process, the nanoPCM experiences phase changing and stores the heat. Because of the heat transfer from the heat source to the nanoPCM, heat source temperature changes over the time.

Immediately after the entirety of nanoPCM melts, the heat generation gets off, see Fig. 1b. At the same time, the temperature of cavity sidewalls (i.e., left and right) is changed to a time-reducing temperature of $Tc(t) = -0.01(Fo - 4.0)$, where Fo is the Fourier number and calculated by the equation of $\alpha_f\, t/l^2$. Following up, the solidification process starts adjacent to the sidewalls. In this study, the Rayleigh and Stefan numbers are constant ($Ra = 5.74 \times 10^5$, $Ste = 0.069$, and $Pr = 1373$) for all cases. Thermophysical properties of paraffin, alumina, and aluminum are given in Table 2.

3 Experimental methodology

3.1 Preparation of paraffin–alumina nanoPCM

To prepare paraffin–alumina nanoPCMs, alumina nanoparticles with the diameter of 20 nm and oleic acid as a surfactant as well as liquid paraffin were weighted by a digital scale with the precision of 0.0001 g. Then, nanoparticles and oleic acid were mixed by a weight ratio of 1:3, respectively. To stabilize the nanoparticles in the fluid, a magnetic stirrer was used for 30 min at the temperature of 70 °C. After that, paraffin was gradually added to the solution. Equation (1) is used to calculate the mass of nanoparticles, surfactant, and paraffin, considering that the samples of 0.01, 0.02, and 0.03 volume fractions of nanoPCM must be prepared. For example, for preparing a 0.02 volume fraction nanofluid, 25, 136.2, and 6.41 g of paraffin, nanoparticles, and surfactant should be mixed, respectively.

$$\phi\% = \frac{(w/\rho)_{np}}{(w/\rho)_{np} + (w/\rho)_{paraffin}} \tag{1}$$

Finally, to achieve a homogeneous distribution of nanoparticles in the PCM, the samples were located in a sonicator bath at 50 °C for about 3 h. The above-mentioned steps were repeated for all samples.

To test the stability of the samples, the Laser Particle Size Analyzer (Vasco Flex-Technique, Arduan, France) was used. This device illustrates the stability of the sample by measuring the size of particles suspended in a base fluid through the dynamic optical spectrum. As it is observed in Fig. 2-left, the highest frequency of particles is in the range of 20 nm, which is equal to the initial diameter of nanoparticles. Had the particles been stuck together, cracked or deposited, the measured frequency would be much larger than the initial size of the base nanoparticles. Figure 2-right depicts that the mean value of the diameters of the coated nanoparticles was distinguished equal to 28.86 nm

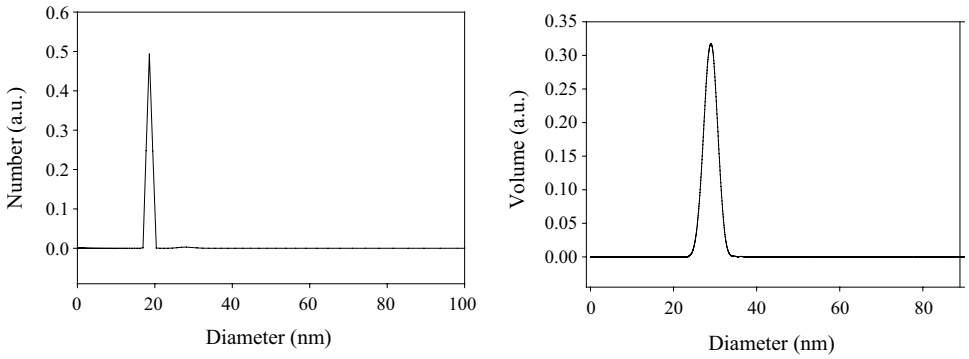

Fig. 2 Left: Particle size distribution of alumina nanoparticles in paraffin, right: measured size distributions of the volume occupied by nanoparticles

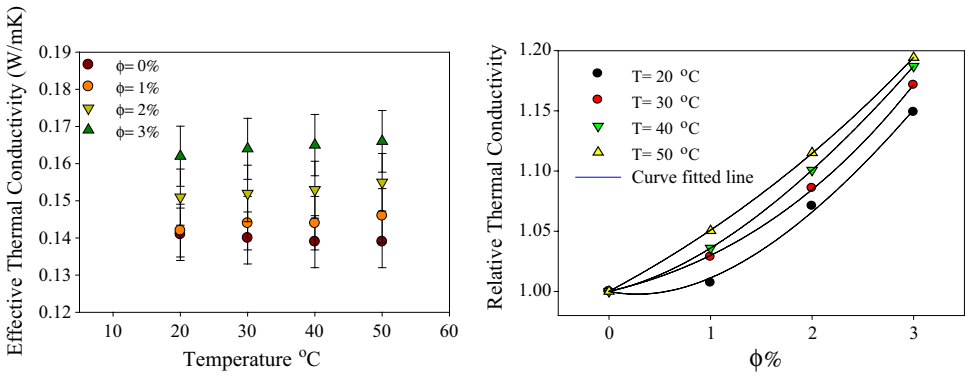

Fig. 3 Left: The measured effective thermal conductivity including the 0.05 uncertainties of the data. Right: the predicted relative thermal conductivity by curve-fitted line and the experimental data at different volume fractions (0–3%) and temperatures (20–50 °C)

with the intensity of 98.95% of all alumina nanoparticles. It means that 98.95% of reflecting nanoparticles are in the range that is near to the size of 28.86 nm. This shows that nanoparticles have not agglomerated or settled at the bottom of the sample, indicating the proper level of stability.

3.2 Thermal conductivity measurement

Using the KD2 Pro device, the effective heat conductivity coefficient can be measured at different temperatures. KD2 Pro is a portable device with a probe sensor which measures the conductivity of the sample material employing the hot-wire method [28]. The temperature of the wire depends on the thermal conductivity of the nanofluid. This temperature is an indicator for thermal conductivity of the sample.

The thermal conductivity coefficient test was carried out for various volume fractions. Each test was repeated five times to reduce the measurement error, and the average of data was calculated. The aim of these tests was to extract the relationship between the thermal conductivity of the nanofluid, the thermal conductivity of the base fluid, the volume fraction, and the temperature. The measured effective thermal conductivity including the 0.05 uncertainty of the data and the relative thermal conductivity as well as the correlated equation (curve-fitted lines) for various volume fractions (0–3%) and different temperatures (20–50 °C) are demonstrated in Fig. 3.

Table 3 Coefficients of a, b, and c values of Eq. (2)

Coefficients	T (°C)			
	20	30	40	50
a	0.14	0.14	0.14	0.14
b	−1.97	−2.11	−2.59	−3.41
c	0.2031	0.192	0.181	0.170

The presented data for relative thermal conductivity (RTC) were translated to the following mathematical equation (Eq. 2):

$$\mathrm{RTC} = \frac{b + a\phi}{b - 2a\phi} + c\phi \tag{2}$$

where a, b, and c are the functions of temperature. Their values are given both in Table 3 and in Eqs. (3) and (4).

To verify the accuracy of the curve-fitted equations, the error function was defined between the measured data and the calculated values. The calculated error values indicate that the maximum error is 1.61, which is an acceptable error.

$$b = -2.7106 + 0.072T - 0.0017T^2 \tag{3}$$

$$c = 0.251 - 0.0011T \tag{4}$$

3.3 Dynamic viscosity measurement

In this section, the measured viscosities resulted by Digital Rheometer (model DV3 made by the American Brookfield Co.) are presented. This device is equipped with a digital display and a warm bath to adjust the temperature. The device provides a viscosity measurement at different temperatures up to 100 °C and different shear rates. The measurement error is reported to be at most 1%; moreover, an error of up to 1% is considered for the temperature of the warm bath based on the device catalog.

The samples poured into the beaker, and the spindle was mounted. The hot bath temperature was adjusted, and after the temperature was stabilized, the viscosity value was reported by the program on the screen. The data were measured at different temperatures from 20 to 60 °C in each 10 °C and for different volume fractions (0, 0.01, 0.02, and 0.03) of nanoparticles.

To evaluate the shear behavior of the nanofluid accurately, the variation of viscosity with temperature and volume fraction of nanoparticles should be determined (see Fig. 4). These values were measured at the shear rate of 200 s^{-1}. At this value, the paraffin–alumina nanoparticle viscosity was observed to be independent of the shear rate. In other words, the shear rate is higher enough that the nanofluid behaves as a Newtonian fluid.

The results show that the viscosity decreases by increasing the temperature. At high temperatures, the viscosity of the base fluid decreases due to the reduction of layer interaction forces within the fluid. In addition, at high temperatures, the probable contact between particles, which obstructs the movement of fluid layers, decreases. By increasing the volume fraction of nanoparticles in the base fluid, the viscosity increases. In fact, that shear stress and friction between fluid layers increase because of the solid nanoparticles interaction [29].

It was observed that the paraffin viscosity is highly dependent on the temperature. Equation (5) with a very high accuracy ($R^2 > 0.99$) is fitted to the pure PCM viscosity data in order to calculate the viscosity as a function of temperature.

$$\mu_o(T) = 0.07193e^{-0.0365T} \tag{5}$$

Figure 5 shows the variation of the relative viscosity versus volume fractions at different temperatures. In order to obtain the suitable equation for prediction of nanofluid viscosity as a function of temperature and volume fraction, many equations were examined on the measured data. Finally, Eq. (6) is obtained giving the best prediction of relative viscosity as a function of temperature and volume fraction of nanoparticles.

$$\frac{\mu_{nf}}{\mu_{bf}} = 1 + \frac{a(e^{b\phi} - 1)}{T} \tag{6}$$

$$a(T) = -0.7792 + 0.3363e^{0.0645T} \tag{7}$$

$$b(T) = 235.5581 - 5.1449T + 0.0913T^2 - 0.0006T^3 \tag{8}$$

The calculated viscosities using Eq. (6) show maximum 4% deviation from the measured data, indicating the accuracy of the proposed equation for the relative viscosity prediction.

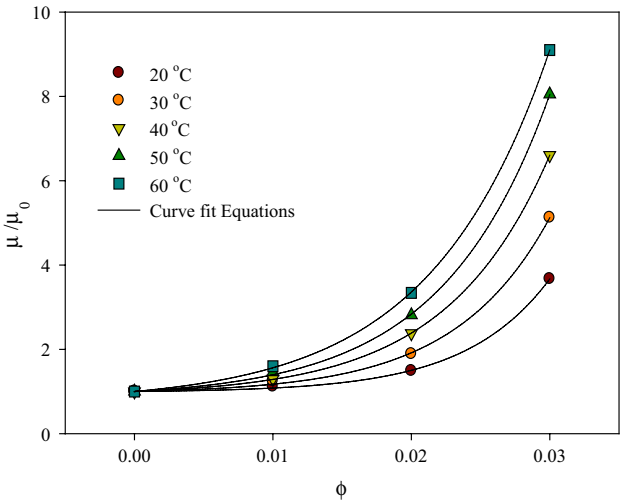

Fig. 5 Relative viscosity versus volume fraction of nanoparticles for various temperatures

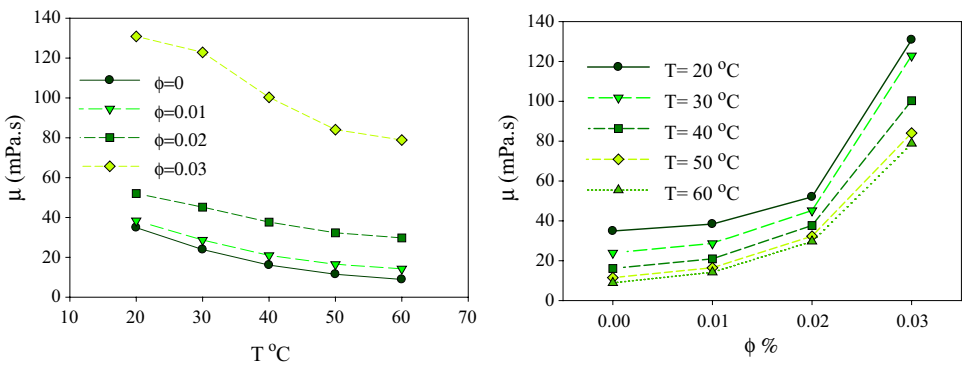

Fig. 4 Dynamic viscosity of nanofluids; left: versus temperature for various volume fractions, right: versus volume fraction for various temperatures

4 Numerical approach

In this section, first, the governing equations are represented both in dimensional and in non-dimensional forms. Then, the boundary and initial conditions are introduced, and finally, the numerical method is comprehensively explained.

4.1 Governing equations

The governing equations describing the natural convection and conduction within the phase-change material are given below [3],

- Continuity:

$$\frac{\partial u}{\partial x}+\frac{\partial v}{\partial y}=0 \tag{9}$$

- x momentum:

$$\frac{\partial u}{\partial t}+u\frac{\partial u}{\partial x}+v\frac{\partial u}{\partial y}=\frac{1}{\rho_{\mathrm{nf}}}\left(-\frac{\partial p}{\partial x}+\mu_{\mathrm{nf}}\nabla^2 u+bu\right) \tag{10}$$

- y momentum:

$$\frac{\partial v}{\partial t}+u\frac{\partial v}{\partial x}+v\frac{\partial v}{\partial y}=\frac{1}{\rho_{\mathrm{nf}}}\left(-\frac{\partial p}{\partial y}+\mu_{\mathrm{nf}}\nabla^2 v+bv+\rho_{\mathrm{nf}}g\beta(T-T_{\mathrm{m}})\right) \tag{11}$$

- Energy (liquid phase):

$$\frac{\partial T}{\partial t}+u\frac{\partial T}{\partial x}+v\frac{\partial T}{\partial y}=\alpha_{\mathrm{nf}}\nabla^2 T-\frac{h_{\mathrm{nf}}}{c_{\mathrm{nf}}}\frac{\partial f}{\partial t} \tag{12}$$

- Energy (solid phase):

$$\frac{\partial T}{\partial t}=\alpha_{\mathrm{ns}}\nabla^2 T \tag{13}$$

- Energy (heat source):

$$\frac{\partial T}{\partial t}=\alpha_{\mathrm{s}}\nabla^2 T+\frac{q'''}{(\rho c_{\mathrm{p}})_{\mathrm{s}}} \tag{14}$$

The density, the specific heat capacity, the expansion coefficient, and the latent heat of nanofluids are calculated based on the corresponding volume fraction of the nanoparticles [17]:

$$\rho_{\mathrm{nf}}=(1-\phi)\rho_{\mathrm{f}}+\phi\rho_{\mathrm{np}} \tag{15}$$

$$(\rho c)_{\mathrm{nf}}=(1-\phi)(\rho c)_{\mathrm{f}}+\phi(\rho c)_{\mathrm{np}} \tag{16}$$

$$(\rho\beta)_{\mathrm{nf}}=(1-\phi)(\rho\beta)_{\mathrm{f}}+\phi(\rho\beta)_{\mathrm{np}} \tag{17}$$

$$h_{\mathrm{nf}}=\frac{(1-\phi)(\rho h)_{\mathrm{f}}}{\rho_{\mathrm{nf}}} \tag{18}$$

The solid-to-liquid phase-change process is mathematically described using the enthalpy-porosity formulation proposed by Brent et al. [30]. In this approach, the parameter b, defined in the momentum equations (Eqs. 10 and 11), gradually reduces the velocities from a finite value in the liquid to zero in the solid phase, over through the computational cell where the phase change is undergoing. This is accomplished by supposing that these cells act like a porous media with a porosity equivalent to the liquid fraction. Based on the Carman–Kozeny relation, the coefficient b is characterized as:

$$b=\frac{-C_1(1-f)^2}{f^3+C_2} \tag{19}$$

In this equation, $f=1$ and $f=0$ belong to the liquid and solid regions, respectively. "f" can take values between 0 and 1 in the mushy zone (liquid and solid). The constant C_1 takes a large value (10^7-10^{15}) to suppress the velocity as the cell behaves like solid, and C_2 takes a small constant to avoid the denominator getting zero when the cell is fully located in the solid region, namely $f=0$. The choice of these constants is arbitrary; however, they must be changed to achieve the convergence of the running code [19]. Accordingly, $C_1=1\times10^8$ kg m^{-3} s^{-1} and $C_2=0.003$ are used in this study.

The governing equations are reduced to the non-dimensional form by using the following variables including dimensionless parameters like $X=x/l, Y=y/l, U=ul/\alpha_{\mathrm{f}}$, $V=vl/\alpha_{\mathrm{f}}, \theta=\left(T-T_{\mathrm{m}}\right)/q'''l^2/k_{\mathrm{s}}, P=pl^2/\rho_{\mathrm{nf}}\alpha_{\mathrm{f}}$, as well as dimensionless governing numbers like $Fo=\alpha_{\mathrm{f}}t/l^2$ which is Fourier number, $B=bl^2/\rho_{\mathrm{nf}}\alpha_{\mathrm{f}}$ is the dimensionless form of b, $Ra=g\beta_{\mathrm{f}}q'''l^5/k_{\mathrm{s}}\nu_{\mathrm{f}}\alpha_{\mathrm{f}}$ is the Rayleigh number, $Ste=c_f q'''l^3/h_{\mathrm{nf}}k_{\mathrm{s}}$ is the Stefan number, $Pr=\nu_{\mathrm{f}}/\alpha_{\mathrm{f}}$ is the Prandtl number.

Continuity:

$$\frac{\partial U}{\partial X}+\frac{\partial V}{\partial Y}=0 \tag{20}$$

X momentum:

$$\frac{\partial U}{\partial \tau}+U\frac{\partial U}{\partial X}+V\frac{\partial U}{\partial Y}=-\frac{\partial P}{\partial X}+\frac{\mu_{\mathrm{nf}}}{\rho_{\mathrm{nf}}\alpha_{\mathrm{f}}}\nabla^2 U+BU \tag{21}$$

Y momentum:

$$\frac{\partial V}{\partial \tau}+U\frac{\partial V}{\partial X}+V\frac{\partial V}{\partial Y}=-\frac{\partial P}{\partial Y}+\frac{\mu_{\mathrm{nf}}}{\rho_{\mathrm{nf}}\alpha_{\mathrm{f}}}\nabla^2 V+\frac{(\rho\beta)_{\mathrm{nf}}}{\rho_{\mathrm{nf}}\beta_{\mathrm{f}}}RaPr\theta+BV \tag{22}$$

Energy (liquid phase):

$$\frac{\partial \theta}{\partial \tau}+U\frac{\partial \theta}{\partial X}+V\frac{\partial \theta}{\partial Y}=\frac{\alpha_{\mathrm{nf}}}{\alpha_{\mathrm{f}}}\nabla^2\theta-\frac{h_{\mathrm{nf}}}{c_{\mathrm{nf}}\Delta T}\left(\frac{\partial f}{\partial \tau}\right) \tag{23}$$

Table 4 The initial and boundary conditions

Case	Initial/boundary conditions
Initial time	$U=V=0$ and $\theta=0$
Horizontal walls	$U=V=0$ and $\frac{\partial\theta}{\partial Y}=0$
Vertical walls	$U=V=0$ and $\frac{\partial\theta}{\partial X}=0$
Liquid–solid interface	$U=V=\theta=0$

Energy (solid phase):

$$\frac{\partial\theta}{\partial\tau}=\frac{\alpha_{ns}}{\alpha_f}\nabla^2\theta \tag{24}$$

Energy (heat source):

$$\frac{\partial\theta}{\partial\tau}=\frac{\alpha_s}{\alpha_f}\nabla^2\theta+\frac{\alpha_s}{\alpha_f} \tag{25}$$

The dimensionless initial and boundary conditions are tabulated in Table 4.

4.2 Numerical method

The governing equations along with the boundary conditions are discretized using control volume method (CVM) [31, 32]. The power law scheme, which is a combination of the central difference and the upwind schemes, is used to discretize the convection terms. The SIMPLE algorithm proposed by Patankar [33] is used to solve the discretized and coupled continuity, momentum and energy equations. Moreover, a line-by-line solver based on the tri-diagonal matrix algorithm (TDMA) is used to solve iteratively the algebraic discretized equations.

In this work, the enthalpy value is expressed as a linear function of temperature [34].

$$h=h_{nf}f+c_{nf}(T_e-T_m)f-c_{ns}(T_m-T_w)(1-f) \tag{26}$$

where f is the liquid fraction and T_e and T_w are the left and right temperatures of the control volume, respectively. Rearranging Eq. (22), the liquid fraction in a control volume is calculated from Eq. (23).

$$f=\frac{h-c_{ns}(T_m-T_w)}{h_{nf}+c_{nf}(T_e-T_m)+c_{ns}(T_m-T_w)} \tag{27}$$

The location of the melting and solidification front is determined by the liquid fraction contour equal to $f=0.5$. This formulation of the enthalpy method remarks a considerable advantages highlighted by previous studies [35].

4.3 Model validation

To validate the developed numerical model, the predicted melting front is compared with measurements of Gau and Viskanta [36] and modeling results of Brent et al. [30]. Their studies were carried out in a rectangular cavity with a length of 88.9 and a width of 63.6 mm. The temperature of the hot and cold walls is $T_h=38$ °C and $T_c=28.3$ °C, respectively. Therefore, the dimension and boundary conditions of the cavity were adapted accordingly, and the results were compared with each other. The comparison is depicted in Fig. 6. As it is observed, the predicted melting front is very close to both the experimental results of Gau and Viskanta [36] and the modeling results of Brent et al. [30]. This comparison proves the reliability of the presented numerical model.

4.4 Grid and time step independency

The effect of the grid number and the time step on the results is investigated to scrutinize the numerical method. For this, the volumetric changes of the liquid phase inside the cavity have been monitoring during the melting process. In Fig. 7, the liquid phase fraction is shown for the different grid numbers and time steps for Rayleigh number equal to 5.74×10^5. Based on the results, a 180×180 network and a time step equal to 0.005 are selected for obtaining the results, precisely.

5 Results and discussion

In this section, first, the phase-change process of the nano-PCM is studied in the form of isotherms and streamlines in the liquid phase during melting and solidification for the various volume fractions of zero, 0.01, and 0.02 of nanoparticles. Second, the effect of adding nanoparticles to the base PCM on the liquid fraction trend versus dimensionless time is discussed for a constant Rayleigh number of 5.74×10^5

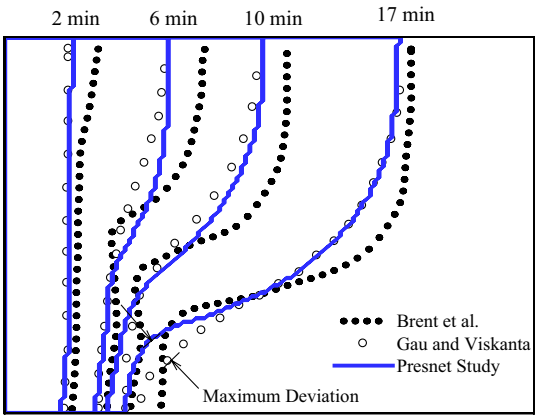

Fig. 6 Comparison between the predicted melting front in the present work, the numerical results of Brent et al. [30] and the measurements of Gau and Viskanta [36]

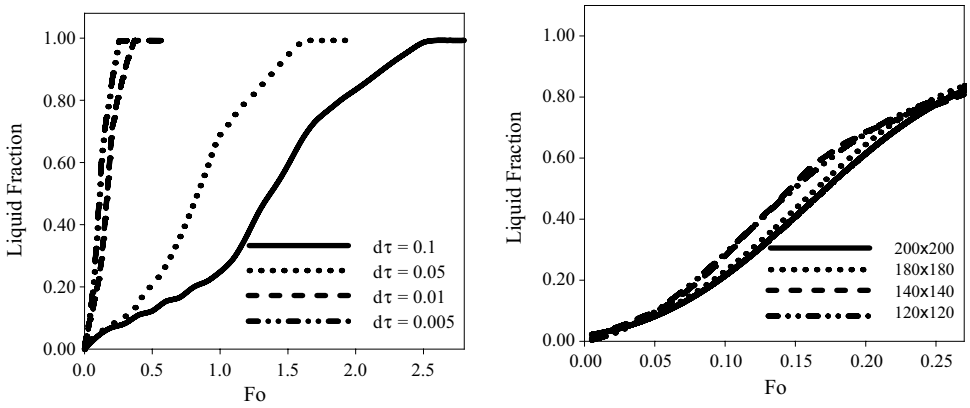

Fig. 7 Left: Time step study, right: grid numbers study at $Ra = 5.74 \times 10^5$

and Stefan number of 0.069 based on the paraffin properties given in Table 2.

Figure 8 shows the streamlines in the liquid region. The salient point of the feature is the axially symmetric form of vortices. At the early stage, there are small vortices around the heat source. At this time, the dominant mode of heat transfer is conduction. Over time, vortices become stronger and occupy a large area at the top of the heat source.

Figure 8 also shows the influence of nanoparticles addition on the streamlines. It can be seen that an increase in the volume fraction of nanoparticles leads to an increase in the heat transfer rate and melting speed. Also, the streamlines formation indicates that at the beginning of the melting, which the role of the conduction heat transfer is dominant, nanoparticles noticeably help to release the heat from the heat source. Therefore, in the middle of the melting period, since the free convection amplifies the heat transfer rate from

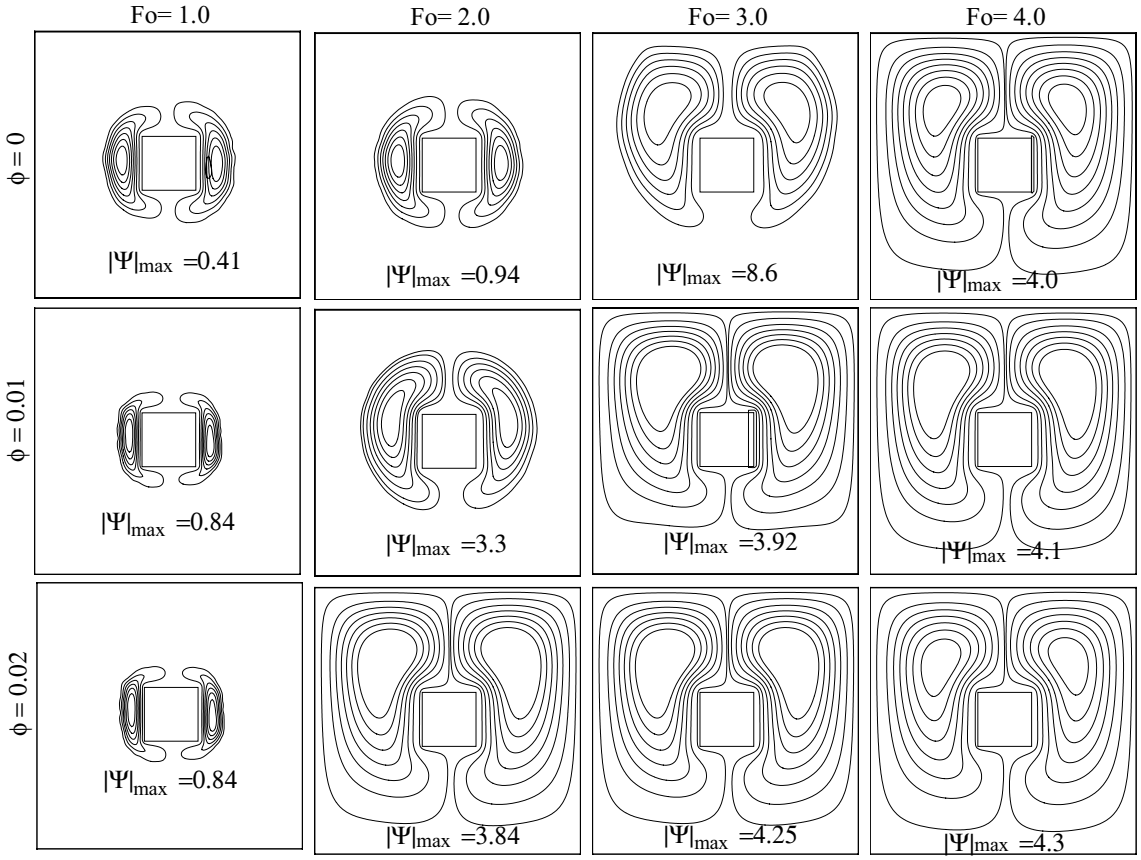

Fig. 8 Streamlines in the molten nanofluid for various volume fractions at different dimensionless times

the source, convective currents extend in a wider space of the cavity.

It should be noted that adding nanoparticles has different effects on fluid behaviors. On the one hand, it enhances the thermal conductivity, which improves the conductive heat transfer rate. On the other hand, it increases the nanofluid viscosity, which dampens the convective currents. An increase in the thermal conductivity, especially where the conduction is dominant, increases the heat transfer and the temperature of the liquid phase. However, it decreases the temperature gradient between the source and the melting front that itself leads to a reduction in the power of vortices in a short period.

The highest value of the stream function for pure paraffin can be seen at $Fo = 3$. At this stage, the vortices move from the sides to the top of the source. Therefore, the liquid phase is limited in an area constrained between the hot wall of the heat source from the bottom and the cold solid phase at the top. Subsequently, the convection currents and the stream function meat their maximum value.

Figure 9 shows isotherm lines in the liquid phase. As we know, the non-dimensional temperature at the melting point is zero, so 0.00 labels marked the melting front. The compact form of isotherm lines near the source indicates a high-temperature gradient over there. Curved line formation of isotherms in the upper part of the molten zone indicates the strong convective currents in this area, while at the lower part, beneath the heat source, the conduction heat transfer is dominant. It can be concluded that for this particular geometry, which the heat source is located at the center of the cavity, the convective heat transfer at the cavity's lower part is not dominant.

The results show that the melting process inside the cavity can be divided into three distinct stages: in the first stage, conduction heat transfer is dominant. This occurs at the early time of the melting. In the second stage, convection plays a major role in heat transfer. In the last stage, over the lower part of, the conductive heat transfer becomes dominant again. The results also show that the melting rate reaches its higher amount at the second stage when the convection heat transfer is significant.

After melting, the heat generation at the heat source gets off and the sidewalls are applied at variable cold temperature. Therefore, solidification starts near the sidewalls and gradually moves firstly to the bottom and then to the middle area of the cavity.

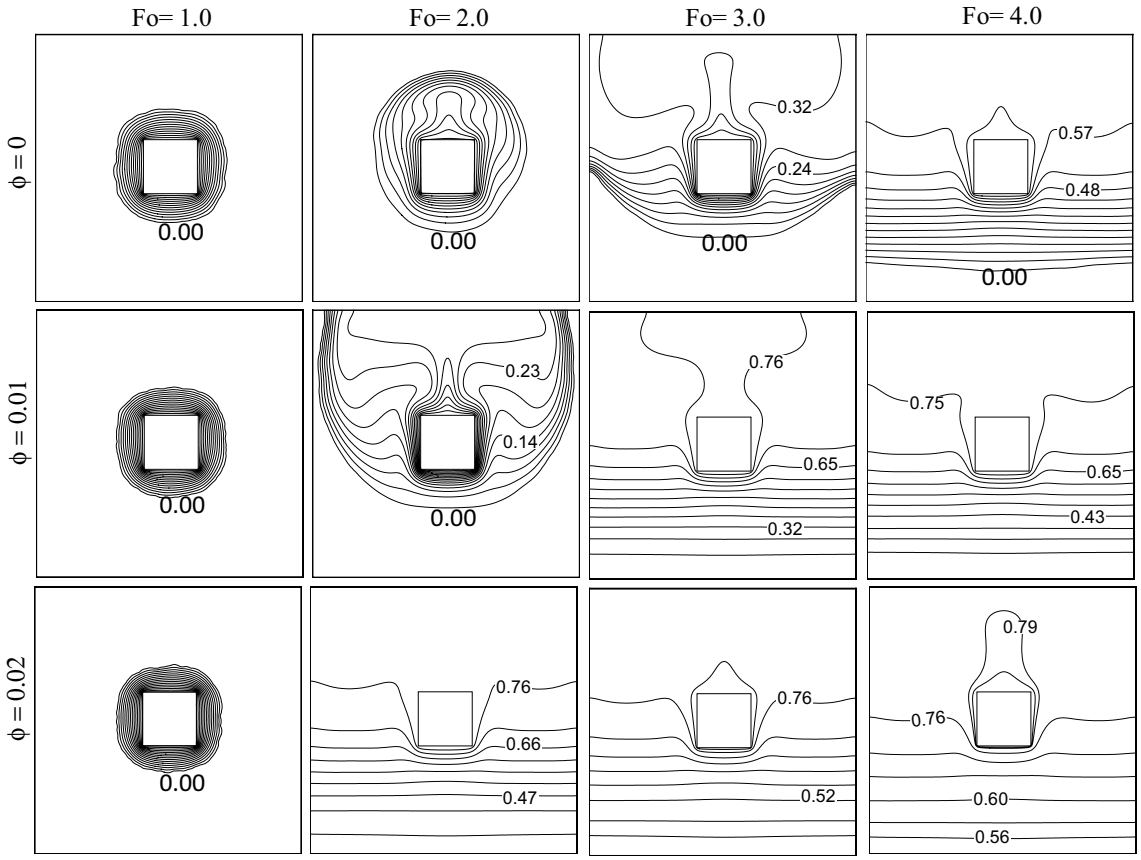

Fig. 9 Isotherm lines in the cavity, for various volume fractions at different dimensionless times

Figure 10 shows streamlines in the liquid phase during the solidification process. The axially symmetric form of vortices is also observed over there. The vortices are created due to a high-temperature gradient between the liquid at the center and the currently solidified phase at both sides. Actually, the cooling downward stream of the liquid near the solidification front and in contrast the hot upward stream at the center lead to a buoyancy-driven flow because of density differences. This causes a heat transfer between the solid and liquid nanoPCMs. The vortices' nucleus moves to the upper part as the solidification proceeds. After a while, the liquid phase and the integrated vortices are limited to an area above the heat source. The liquid above the source is the last part of nanomaterial that is solidified.

During the solidification process, stream functions reach higher values than the similar circumstances in the melting process. The reason lays in the higher-temperature gradient. This value intensifies remarkably at the end of the solidification due to a high-temperature gradient between the source and the solid phase in a small space.

The isotherm lines during the solidification process are shown in Fig. 11 for different volume fractions and various times. The compact form of lines along the cold walls at the initial time of solidification indicates a high-temperature gradient through the region. As the solidification progresses and the front approaches the middle of the cavity, the density of isotherm lines dwindles somewhat. Besides, the curved style of lines is observed near the sidewalls of the source, indicating a high-temperature gradient and a great heat transfer rate over there. An increase in the nanoparticles volume fraction results in a more powerful conductive heat transfer in the solidified phase. The figure also shows the solidification front moving marked with zero value.

It can also be seen that the solidification rapidly begins in a thin layer near the sidewalls and then gets thicker through the bottom of the cavity. The higher rate of solidification alongside the sidewalls at the bottom of the cavity is because of two reasons: first; it is adjacent to the cold source where the temperature gradient is high; second; it locates at the furthest location from the heat source (during the melting period), where it has the lowest temperature.

Figure 12 shows the liquid fraction of nanoPCM as a function of the dimensionless time for the various volume fractions (φ = zero, 0.01, 0.02, and 0.03) of paraffin–alumina. These results indicate that by increasing the volume fraction of nanoparticles up to 0.01, the melting rate

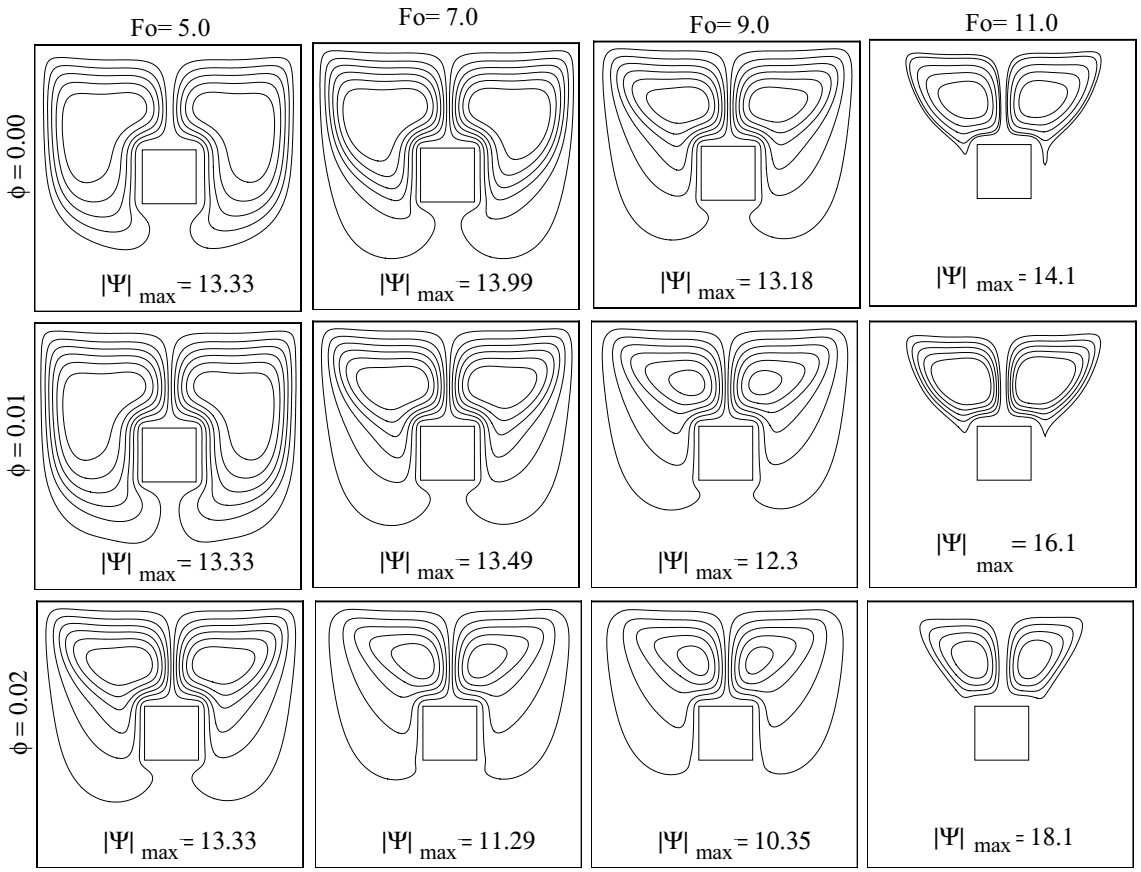

Fig. 10 Streamlines during the solidification for different volume fractions and dimensionless times

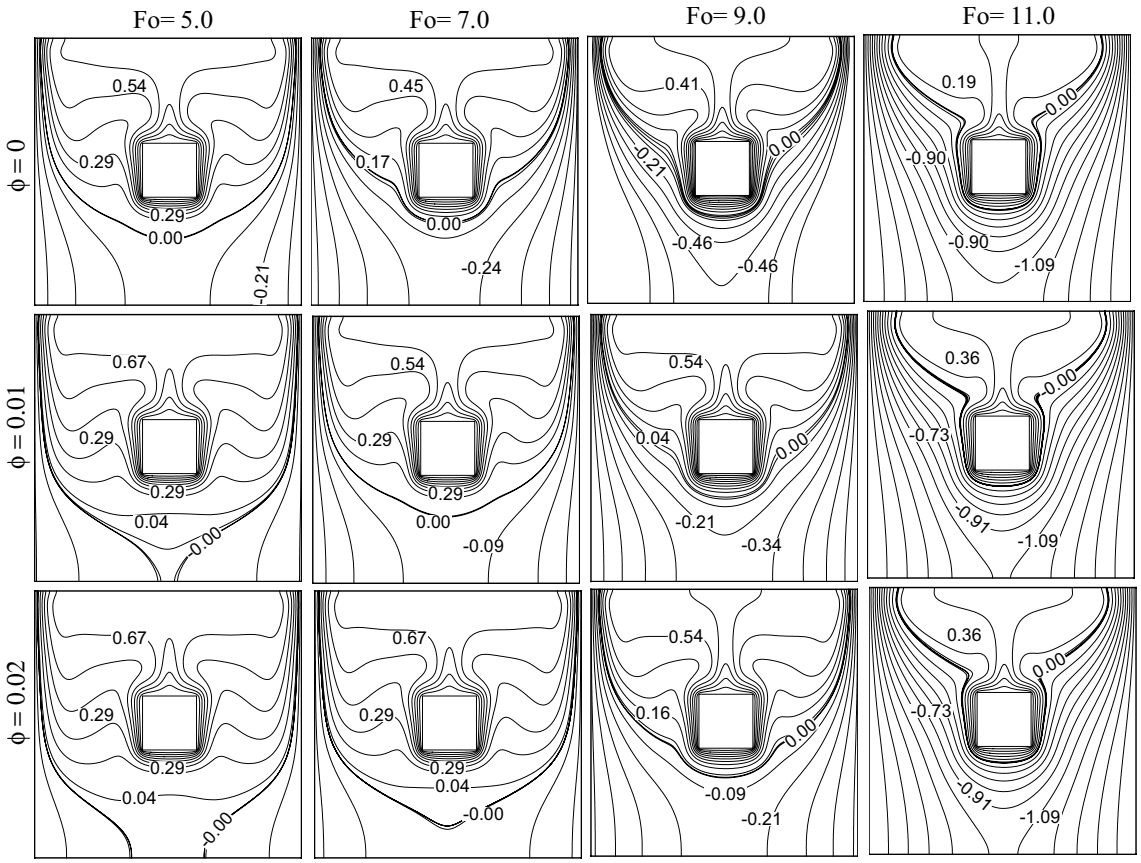

Fig. 11 Isotherm lines for various volume fractions at different dimensionless times during solidification

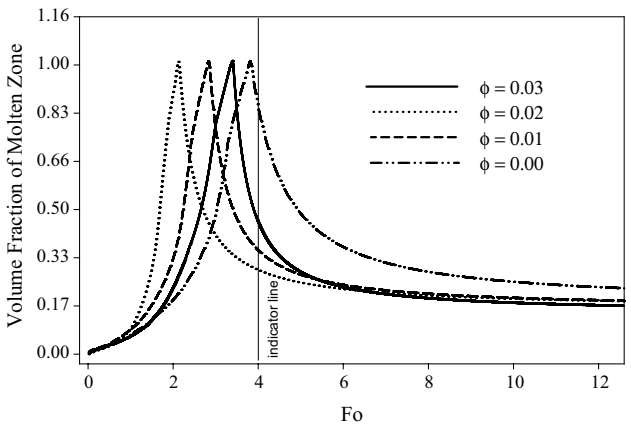

Fig. 12 Liquid fraction of nanoPCM versus dimensionless time for various volume fractions of nanoPCMs

increases by 1.5 times. It also shows that any increase in the volume fraction up to 0.02 leads to an increase in melting rate. This drives from an increase in the thermal conductivity of nanoPCMs. As a result, at the time of $Fo = 2$, about 30% and 95% of the PCM were melted for $\varphi = 0.01$ and 0.02, respectively, while the corresponding value for pure paraffin is about 20%. It means that for the volume fraction of 0.02 the melting rate improves by more than three times. Accordingly, at the time of $Fo = 4$ (see the indicator line in Fig. 12), the nanofluid of 0.01, 0.02, and 0.03 has reached to 75%, 80%, and 52% of their overall process, respectively.

The melting rate of the volume fraction of 0.03 is surprisingly less than that is observed for 0.01 and 0.02 and is higher than that for the pure paraffin. This behavior is due to the increase in the nanofluid viscosity of concentrated nanofluid, which dampens the buoyancy-driven forces as well as natural convection currents [27].

An increase in the volume fraction of nanoparticles significantly improves the conduction type of heat transfer; therefore, for all cases, the solidification rate is higher than that for the base material, especially when keeping in mind that the only heat transfer mechanism between the cold walls and the solidification front is just conduction.

However, the solidification rate gradually decreases during the time for all cases of nanomaterials. It is due to the increase in the thickness of the solidification layer adjacent to the cold walls. Therefore, the nanoPCM with the volume

fraction of 0.03 provides the highest solidification rate. Overall, taking into account the overall successive melting and solidification, the volume fractionation of 0.02 represents the fastest performance in terms of the charging and discharging rate.

The thicker the layer of solidification, the more the reduction in the heat release rate from the liquid nanomaterial to the sidewalls. Therefore, after a long time, a mass of nanoPCM remains liquid at the center area. This self-insulating feature in the solidification process is an important issue and must be considered, especially in larger cavities. Accordingly, as shown in Fig. 12, the time of solidification is remarkably more than the time of melting. Subsequently, the nanoPCM at the top of the heat source remains liquid after a while, as shown in Fig. 10.

6 Conclusion

In this work, the effect of nanoparticles of alumina on the successive melting and solidification of paraffin in a cavity heated from an aluminum heat source was numerically investigated. The governing equations including Navier–Stokes and energy conservation for nanoPCM as well as the heat source were discretized using CVM.

The thermal conductivity and viscosity of nanoPCMs experimentally measured, curve-fitted, and examined based on the nanoparticles volume fraction and temperature.

The SIMPLE algorithm coupled with the enthalpy-porosity method was used to solve numerically the equations and modeling the process of melting and solidification phase change, respectively. Streamlines, isotherms, melting and solidification rates were presented for the different volume fractions of nanoparticles.

It has been observed that in this particular geometry, which the thermal source locates at the center of a cavity, the melting process can be divided into three stages, in which one of the heat transfer mechanisms plays a major role. The first stage forms at the early time of the melting close to the hot source walls. In this case, conduction is the dominant heat transfer mechanism. The next step is the melting at the middle and at the upper part of the cavity, where convection heat transfer plays the main role. The final stage occurs at the lower part of the cavity, where the conduction heat transfer is dominant again. This study showed that the design of the thermal storage devices should be done according to the predominant mechanisms of the heat transfer (i.e., convection and conduction).

The results also show the dominant mechanism of the heat transfer is conduction at the early time and adjacent to the thermal source. Therefore, an increase in the nanoparticles volume fraction improves the melting rate. As melting develops more and more, the convection plays a major role in the heat transfer; at this stage, an increase in the volume fraction causes a reduction in the heat transfer rate and, consequently, the melting rate.

The highest rate of the melting of paraffin–alumina was found to be for the volume fraction of 0.02; at this case, a conduction increase derived from the addition of nanoparticles overcomes the reduction of convective heat transfer due to the increased viscosity. Meanwhile, the highest solidification rate is achieved for the volume fraction of 0.03. However, a significant result reveals when considering the overall melting and solidification process: The nanofluid with the volume fraction of 0.02 represents the best heat transfer rate meaning the shortest time of charging and discharging.

The other important point is the self-insulating phenomenon observed in the solidification process. Therefore, the solidification process prolonged in a significant scale compared to the melting time. This phenomenon must be considered, especially in the design of a LHTES.

Compliance with ethical standards

Conflict of interest The authors declare that there is no conflict of interest.

References

1. Alva G, Liu L, Huang X, Fang G (2017) Thermal energy storage materials and systems for solar energy applications. Renew Sustain Energy Rev 68:693–706
2. Py X, Azoumah Y, Olives R (2013) Concentrated solar power: current technologies, major innovative issues and applicability to West African countries. Renew Sustain Energy Rev 18:306–315
3. Agyenim F, Hewitt N, Eames P, Smyth M (2010) A review of materials, heat transfer and phase change problem formulation for latent heat thermal energy storage systems (LHTESS). Renew Sustain Energy Rev 14:615–628
4. De Souza S, Vielmo HA (2005) Numerical analysis of water melting and solidification in the interior of tubes. J Braz Soc Mech Sci Eng 27:119–131
5. Tian Y, Zhao C-Y (2013) A review of solar collectors and thermal energy storage in solar thermal applications. Appl Energy 104:538–553
6. Xu B, Li P, Chan C (2015) Application of phase change materials for thermal energy storage in concentrated solar thermal power plants: a review to recent developments. Appl Energy 160:286–307
7. Jourabian M, Farhadi M, Darzi AR (2012) Simulation of natural convection melting in an inclined cavity using lattice Boltzmann method. Sci Iran 19:1066–1073
8. Babapoor A, Karimi G (2015) Thermal properties measurement and heat storage analysis of paraffinnanoparticles composites phase change material: comparison and optimization. Appl Therm Eng 90:945–951
9. Khodadadi J, Hosseinizadeh S (2007) Nanoparticle-enhanced phase change materials (NEPCM) with great potential for

improved thermal energy storage. Int Commun Heat Mass Transf 34:534–543
10. Hu N, Zhu Z-Q, Li Z-R, Tu J, Fan L-W (2018) Close-contact melting heat transfer on a heated horizontal plate: revisited in the presence of nano-enhanced phase change materials (NePCM). Int J Heat Mass Transf 124:794–799
11. Sheikholeslami M (2018) Numerical simulation for solidification in a LHTESS by means of Nano-enhanced PCM. J Taiwan Inst Chem Eng 86:25–41
12. Iachachene F, Haddad Z, Oztop HF, Abu-Nada E (2019) Melting of phase change materials in a trapezoidal cavity: Orientation and nanoparticles effects. J Mol Liq 318:441–450
13. Sheikholeslami M, Mahian O (2019) Enhancement of PCM solidification using inorganic nanoparticles and an external magnetic field with application in energy storage systems. J Clean Prod 215:963–977
14. Dadvand A, Boukani NH, Dawoodian M (2018) Numerical simulation of the melting of a NePCM due to a heated thin plate with different positions in a square enclosure. Therm Sci Eng Prog 7:248–266
15. Feng Y, Li H, Li L, Bu L, Wang T (2015) Numerical investigation on the melting of nanoparticle-enhanced phase change materials (NEPCM) in a bottom-heated rectangular cavity using lattice Boltzmann method. Int J Heat Mass Transf 81:415–425
16. Arıcı M, Tütüncü E, Kan M, Karabay H (2017) Melting of nanoparticle-enhanced paraffin wax in a rectangular enclosure with partially active walls. Int J Heat Mass Transf 104:7–17
17. Sebti SS, Mastiani M, Mirzaei H, Dadvand A, Kashani S, Hosseini SA (2013) Numerical study of the melting of nano-enhanced phase change material in a square cavity. J Zhejiang Univ Sci A 14:307–316
18. Farsani RY, Raisi A, Nadooshan AA, Vanapalli S (2017) Does nanoparticles dispersed in a phase change material improve melting characteristics? Int Commun Heat Mass Transf 89:219–229
19. Darzi AR, Farhadi M, Jourabian M (2013) Lattice Boltzmann simulation of heat transfer enhancement during melting by using nanoparticles. Iran J Sci Technol Trans Mech Eng 37:23
20. Boukani NH, Dadvand A, Chamkha AJ (2018) Melting of a Nano-enhanced Phase Change Material (NePCM) in partially-filled horizontal elliptical capsules with different aspect ratios. Int J Mech Sci 149:164–177
21. Kashani S, Ranjbar A, Madani M, Mastiani M, Jalaly H (2013) Numerical study of solidification of a nano-enhanced phase change material (NEPCM) in a thermal storage system. J Appl Mech Tech Phys 54:702–712
22. Khodadadi J, Fan L (2009) Expedited freezing of nanoparticle-enhanced phase change materials (NEPCM) exhibited through a simple 1-D stefan problem formulation. In: ASME Summer Heat Transfer Conference, San Francisco, CA, July, 2009, pp 19–23
23. Maxwell JC (1881) A treatise on electricity and magnetism. Clarendon Press, Oxford
24. Kumar S, Bhoopal RS, Sharma PK, Beniwal RS, Singh R (2011) Non-linear effect of volume fraction of inclusions on the effective thermal conductivity of composite materials: a modified Maxwell model. Open J Compos Mater 1:10
25. Vand V (1948) Viscosity of solutions and suspensions. I. Theory. J Phys Chem 52:277–299
26. Mózes G (1983) Paraffin products. Elsevier, Amsterdam
27. Arasu AV, Mujumdar AS (2012) Numerical study on melting of paraffin wax with Al_2O_3 in a square enclosure. Int Commun Heat Mass Transf 39:8–16
28. Hammerschmidt U, Sabuga W (2000) Transient hot wire (THW) method: uncertainty assessment. Int J Thermophys 21:1255–1278
29. Shahsavar A, Bahiraei M (2017) Experimental investigation and modeling of thermal conductivity and viscosity for non-Newtonian hybrid nanofluid containing coated CNT/Fe_3O_4 nanoparticles. Powder Technol 318:441–450
30. Brent A, Voller V, Reid K (1988) Enthalpy-porosity technique for modeling convection-diffusion phase change: application to the melting of a pure metal. Numer Heat Transf Part A Appl 13:297–318
31. Hunter L, Kuttler J (1989) The enthalpy method for heat conduction problems with moving boundaries. J Heat Transf Trans ASME 111:239–242
32. Zerroukat M, Chatwin CR (1994) Computational moving boundary problems. Research Studies Press, Baldock
33. Patankar S (1980) Numerical heat transfer and fluid flow. CRC Press, Boca Raton
34. Voller V, Swaminathan C, Thomas BG (1990) Fixed grid techniques for phase change problems: a review. Int J Numer Methods Eng 30:875–898
35. Date A (1991) A strong enthalpy formulation for the Stefan problem. Int J Heat Mass Transf 34:2231–2235
36. Gau C, Viskanta R (1986) Melting and solidification of a pure metal on a vertical wall. J Heat Transf 108:174–181